AUTONOMOUS MATERIAL DECOMPOSITION FOR HYPERSPECTRAL NEUTRON TOMOGRAPHY

Mohammad Samin Nur Chowdhury[1], *Diyu Yang*[1], *Shimin Tang*[2], *Singanallur V. Venkatakrishnan*[2], *Hassina Z. Bilheux*[2], *Gregery T. Buzzard*[3], *and Charles A. Bouman*[1]

[1]School of Electrical and Computer Engineering, Purdue University, West Lafayette, IN 47907, USA
[2]Oak Ridge National Laboratory, Oak Ridge, TN 37830, USA
[3]Department of Mathematics, Purdue University, West Lafayette, IN 47907, USA.

ABSTRACT

Hyperspectral neutron tomography is an effective method for analyzing multi-material samples with complex compositions in a non-destructive manner. Since the counts in the hyperspectral neutron radiographs directly depend on the nuclear cross-sections, materials may exhibit contrasting neutron responses across wavelengths. Therefore, it is possible to extract the unique signatures associated with each material and use the signatures to separate the materials simultaneously.

We introduce a fast and effective algorithm to automatically characterize and localize different materials with contrasting neutron responses from the hyperspectral data without prior knowledge. The algorithm estimates the spectra of linear attenuation coefficients from the measured radiographs. It further uses these to perform material decomposition on the data and produces 3D material reconstructions to localize materials in the spatial domain. We achieved promising results for both simulated and real data using the proposed algorithm.

Index Terms— neutron computed tomography, material decomposition, non-negative matrix factorization, clustering, linear attenuation coefficient

1. INTRODUCTION

Neutron tomography has enormous potential for analyzing elemental compositions within objects. It can be particularly valuable in identifying foreign materials or contamination inside a sample [1]. In addition, neutron tomography can be used to monitor the aging of polymers and study the effect of environmental factors on material properties [2]. Also, neutrons interact directly with the nucleus rather than the electron shell. So, neutron tomography provides unique complementary information about a sample compared to conventional techniques like X-ray computed tomography (CT) [3].

Pulsed spallation neutron sources [4] and high-efficiency time-of-flight detectors [5] have enabled us to resolve neutron radiographs into hyperspectral radiographs. This is achieved by distinguishing neutrons with different wavelengths based on their arrival time at the detector. While acquiring hyperspectral radiographs for polycrystalline materials within the thermal and cold neutron wavelength range (0.5 to 10 Angstroms), the incident beams scatter according to Bragg's law. So, the neutron transmission spectra exhibit distinct characteristic fluctuations in intensity corresponding to the Bragg edges for all the crystallographic phases in these materials [6]. This phenomenon enables us to separate different polycrystalline materials in a sample.

Material decomposition for spectral CT is a relatively less explored territory, and most of the existing approaches in the literature are dedicated to x-ray CT. A primary difference among prevailing methods for x-ray CT is in the domain (sinogram or reconstruction) chosen to perform material decomposition [7, 8, 9]. For neutron tomography, a few studies demonstrated material decomposition using neutron absorption resonances in known cross-section spectra for different isotopes within epithermal energy region [10, 11]. A recent work adopted a method of computing linear attenuation coefficients (LAC) for polycrystalline materials utilizing known material locations in the hyperspectral reconstructions and using them for material decomposition [12].

In this paper, we present a novel algorithm to perform automated material decomposition on hyperspectral neutron data without prior information. The algorithm is primarily devoted to Bragg edge imaging but can potentially be used for resonance imaging with minor modifications. Apart from the traditional hyperspectral tomographic techniques, our algorithm embodies two critical steps that enable us to automate material decomposition in a computationally efficient manner. The first one involves a dimensionality reduction procedure that transforms the high-dimensional hyperspectral projections into low-dimensional subspace projections, drastically reducing the volumetric reconstruction requirements. The other step includes an unsupervised clustering

This manuscript has been authored by UT-Battelle, LLC, under contract DE-AC05-00OR22725 with the US Department of Energy (DOE). G. Buzzard was partially supported by NSF CCF-1763896, and C. Bouman was partially supported by the Showalter Trust.

procedure that automatically segments the material regions used for LAC spectra estimation. We implemented our algorithm on both simulated and real data, which allowed us to conduct quantitative and qualitative performance evaluations.

2. METHODOLOGY

Our algorithm calculates LAC spectra and material reconstructions from hyperspectral neutron radiographs. It first reduces noise from the open beams (also known as blank scans or flat fields) and uses them to normalize object projections. The algorithm then decomposes the normalized hyperspectral projections into subspace basis vectors and subspace projections. After that, it reconstructs the subspaces and performs clustering operation to spatially segment material regions. The algorithm then calculates the individual LAC spectrum based on the mean voxel values across the subspaces for each material region. Once the LAC spectra are computed, it performs projection domain material decomposition and finally reconstructions the materials. The entire procedure is divided into seven steps, as shown in figure 1.

2.1. Open Beam Processing

We aim to achieve the highest signal-to-noise ratio (SNR) possible for the open beams. So, we first implement averaging over multiple open beam sets to reduce the noise. Then we filter the open beam images at each wavelength using a 2D normalized hamming window for further smoothing. This operation can be expressed as 2D convolution given by

$$y^o_{r,c,k} = \sum_{i=-\infty}^{\infty} \sum_{j=-\infty}^{\infty} \bar{y}^o_{i,j,k} h_{r-i,c-j} \tag{1}$$

where $y^o \in \mathbb{R}^{N_r \times N_c \times N_k}$ is the smooth open beam array, $\bar{y}^o \in \mathbb{R}^{N_r \times N_c \times N_k}$ is the averaged open beam array, N_r is the number of rows in the detector, N_c is the number of columns in the detector, and N_k is the number of energies/wavelengths.

2.2. Projection Density Computation

To go from neutron counts to projection densities, we need to compute the negative log of the ratios of the object projections and the corresponding open beams. Ideally, the object projections and the open beams would have the same neutron dosage rate, and the background counts would match. But in actual experiments, it can vary inordinately. Let's assume object projections are scaled by $\alpha_{v,k}$, which depends on view and energy. Then we can express the relationship as

$$\hat{p}_{v,r,c,k} = -\log\left(\frac{\alpha_{v,k} y_{v,r,c,k}}{y^o_{r,c,k}}\right) \tag{2}$$

$$\hat{p}_{v,r,c,k} = -\log\left(\frac{y_{v,r,c,k}}{y^o_{r,c,k}}\right) - \log(\alpha_{v,k}) \tag{3}$$

$$\hat{p}_{v,r,c,k} = p_{v,r,c,k} + b_{v,k} \tag{4}$$

$$p_{v,r,c,k} = \hat{p}_{v,r,c,k} - b_{v,k} \tag{5}$$

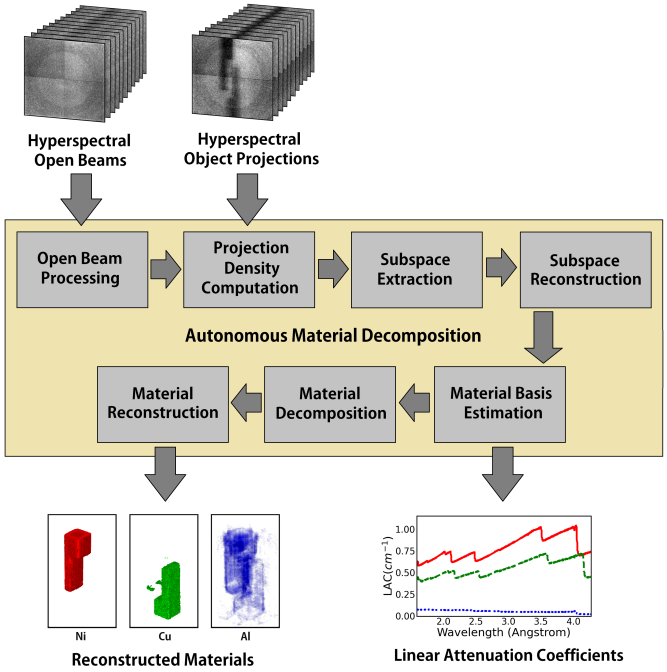

Fig. 1. Illustration of the autonomous material decomposition pipeline with sample inputs (hyperspectral neutron counts) and outputs (LAC, reconstructed materials).

where $p \in \mathbb{R}^{N_v \times N_r \times N_c \times N_k}$ is the ideal projection density array, $\hat{p} \in \mathbb{R}^{N_v \times N_r \times N_c \times N_k}$ is the uncalibrated projection density array, $b \in \mathbb{R}^{N_v \times N_k}$ is the background offset array, $y \in \mathbb{R}^{N_v \times N_r \times N_c \times N_k}$ is the ideal object projection array, and N_v is the number of projection views. So, these background offsets need to be separately calculated and subtracted from the uncalibrated projection densities to make them ideal.

2.3. Subspace Extraction

To acquire a lower dimensional representation of the hyperspectral projection densities, we perform subspace extraction using non-negative matrix factorization (NMF) [13]. NMF can decompose the normalized projections into a set of subspace basis vectors and corresponding subspace projections. The resulting matrices can be obtained by solving the optimization problem given by

$$(V^{s^*}, D^{s^*}) = \arg \min_{(V^s \geq 0, D^s \geq 0)} \{\|p - V^s (D^s)^T\|^2\} \tag{6}$$

where $p \in \mathbb{R}^{N_p \times N_k}$ is the matrix form of the hyperspectral projection densities, $D^s \in \mathbb{R}^{N_k \times N_s}$ is the subspace basis matrix, $V^s \in \mathbb{R}^{N_p \times N_s}$ is the corresponding subspace projection matrix, $N_p = N_v \times N_r \times N_c$ is the number of pixels, and N_s is the number of subspaces. These subspace projections and basis vectors combined preserve all the necessary information. If N_m is the number of materials, then N_s is chosen such that $N_m < N_s << N_k$. So, subspace reconstruction is

significantly faster than hyperspectral reconstruction.

2.4. Subspace Reconstruction

Space domain analysis requires us to perform volumetric reconstructions. Thanks to the reduced dimensions, we can generate high-quality subspace reconstructions within a reasonable time using SVMBIR, a sophisticated python package for super-voxel-based iterative reconstruction [14]. The reconstruction works by solving the optimization problem given by

$$\hat{x}^s = \arg\min_{x^s}\{f(x^s) + h(x^s)\} \tag{7}$$

where $\hat{x}^s$ is the reconstructed subspace image, $f(x^s)$ is the forward model term and $h(x^s)$ is the prior model term. The super-voxel algorithm is then used to efficiently perform this optimization. The forward model term has the form

$$f(x^s) = \frac{1}{2\sigma_v^2}\|V^s - Ax^s\|_\Lambda^2 \tag{8}$$

where x^s is the unknown subspace image to be reconstructed, A is the linear projection operator, Λ is the diagonal matrix of sinogram weights, and σ_v is a parameter controlling the assumed standard deviation of the measurement noise. We used Q-Generalized Gaussian Markov random field (QGGMRF) as the prior model $h(x^s)$.

2.5. Material Basis Estimation

The subspace basis vectors can be transformed into the material basis vectors using a simple transformation matrix $T \in \mathbb{R}^{N_m \times N_s}$ that contains the material weights across the subspace reconstructions. To understand the concept better, we have to go backward. Let's assume that the reconstructed material images x^m are in units of the fraction of volume. That means a voxel fully containing the material is one and is zero if the material is absent. So, each reconstruction in x^s can be represented as a weighted combination of all the reconstructions in x^m. If we store these weights in T, then multiplying x^m with T gives us x^s. From this, we can deduce

$$x^m T = x^s \tag{9}$$
$$A^{-1}V^m T = A^{-1}V^s \tag{10}$$
$$V^m T = V^s \tag{11}$$

where $V^m \in \mathbb{R}^{N_p \times N_m}$ is the material projection matrix. Now both subspace decomposition and material decomposition represent the same hyperspectral projection densities. So, we can say

$$V^s(D^s)^T = p = V^m(D^m)^T \tag{12}$$
$$V^m T(D^s)^T = V^m(D^m)^T \tag{13}$$
$$(D^m)^T = T(D^s)^T \tag{14}$$
$$D^m = D^s T^T \tag{15}$$

Table 1. NRMSE values for the outputs.

Output Type	NRMSE		
	Ni	Cu	Al
LAC	0.005	0.01	0.205
Reconstruction	0.056	0.07	0.765

where $D^m \in \mathbb{R}^{N_k \times N_m}$ is the material basis matrix. However, to compute T, we first need to know the material regions in x^s. In our algorithm, we used GMCluster, a Gaussian mixture model-based clustering package, to estimate the cluster parameters and segment the material regions. Then we can compute the mean voxel values across the subspaces for each region and calculate T. Once we estimate D^m using D^s and T, we can have the LAC spectra by scaling D^m with a factor of $\frac{1}{\delta}$, where δ is the voxel thickness/pixel pitch.

2.6. Material Decomposition

To perform material decomposition, we need to rerun NMF on the projection densities. However, this time, we calculate only V^m using fixed D^m. The optimization problem is given by

$$V^{m^*} = \arg\min_{V^m \geq 0}\{\|p - V^m(D^m)^T\|^2\} \tag{16}$$

2.7. Material Reconstruction

Using the same reconstruction method from section 2.4, the algorithm finally reconstructs our material volumes using the decomposed material projections.

3. RESULTS

Both simulated and real data contain neutron radiographs from 1200 wavelength bins between 1.5 to 4.5 Angstroms, representing a sample with nickel (Ni), copper (Cu), and aluminum (Al). We used 64×64 radiographs for simulated data and 512×512 for real data. The numbers of projection angles are 32 and 27 for simulated and real data, respectively.

Data simulation was performed by combining theoretical LAC spectra with pre-defined material volumes. We computed the theoretical LAC spectra using the Bragg-edge modeling (bem) library [15]. Also, we used the Poisson noise model to make the data realistic. Figures 2 and 3 compare ground truths with estimated outputs (LAC spectra and volumetric slices) for Ni, Cu, and Al. Table 1 provides a quantitative performance analysis in terms of normalized root mean square errors (NRMSE). Finally, 3D visualizations of the reconstructed materials are shown in figure 4.

LAC spectra and reconstructed material slices estimated from the real data are shown in figures 2 (c) and 5. Unfortunately, we can't perform any quantitative analysis on these results as the ground truths are unavailable. Figure 6 shows 3D visualizations of the reconstructed materials.

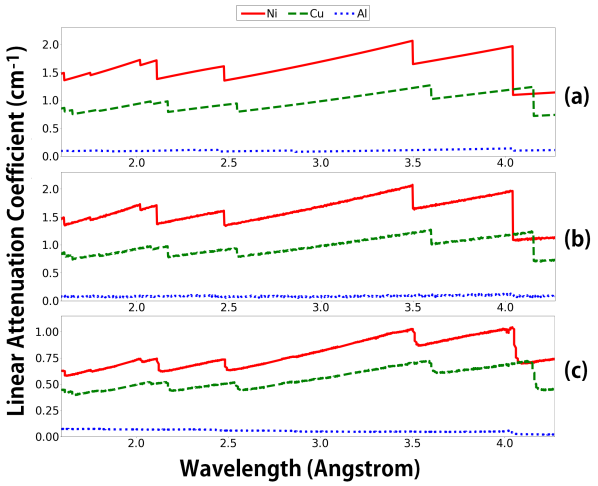

Fig. 2. LAC spectra for Ni, Cu, and Al: (a) used as ground truth for data simulation, (b) estimated by our algorithm from simulated data, (c) estimated by our algorithm from real data.

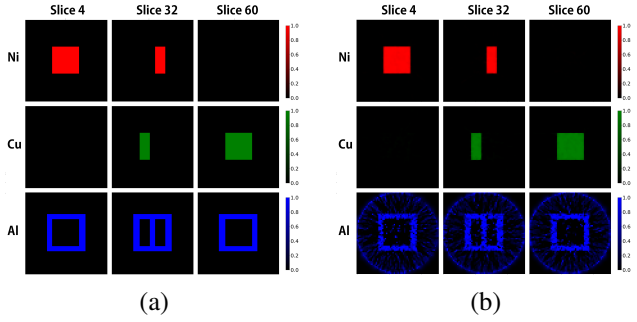

Fig. 3. Different slices for Ni, Cu, and Al in the space domain: (a) used as ground truth for data simulation, (b) estimated by our algorithm from simulated data.

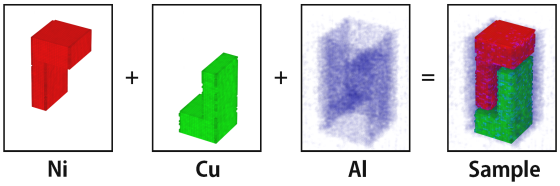

Fig. 4. 3D visualization of the reconstructed Ni, Cu, and Al estimated by our algorithm from simulated data.

4. CONCLUSION

The dimension reduction procedure and the unsupervised clustering approach introduced in our algorithm enabled fast and automated material decomposition for hyperspectral neutron data. Our algorithm produced close to accurate LAC spectra and material volumes for Ni and Cu from both qualitative and quantitative perspectives. The outputs for Al are not as good in comparison, which is expected as Al has a weak presence in neutron radiographs. However, our approach also has some limitations. For the algorithm to work best, the samples' materials must be well separated, i.e., each voxel has to represent a single material. In addition, the density of each material has to be uniform across the sample to make the clustering work properly. Also, the algorithm's performance may vary based on the hyper-parameter values used in different steps. We plan to work on these shortcomings and make the algorithm more generalized.

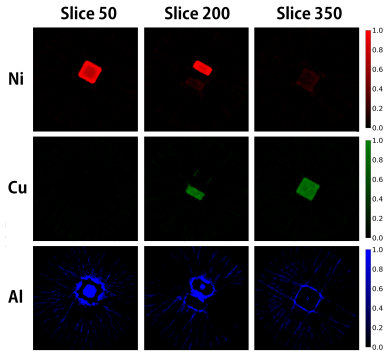

Fig. 5. Different slices for Ni, Cu, and Al in the space domain estimated by our algorithm from real data.

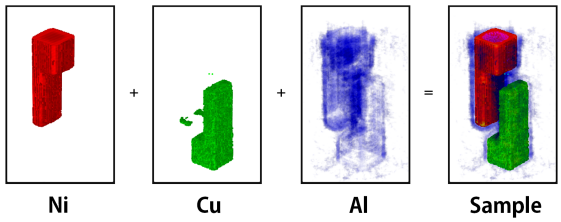

Fig. 6. 3D visualization of the reconstructed Ni, Cu, and Al estimated by our algorithm from real data.

5. ACKNOWLEDGMENTS

A portion of this research used resources at the Spallation Neutron Source, a DOE Office of Science User Facility operated by the Oak Ridge National Laboratory. Oak Ridge National Laboratory is managed by UT-Battelle, LLC, for the U.S. DOE under contract DE-AC05-00OR22725.

6. REFERENCES

[1] K. H. Kim, R. T. Klann, and B. B. Raju, "Fast neutron radiography for composite materials evaluation and testing," *Nuclear Instruments and Methods in Physics Research Section A: Accelerators, Spectrometers, Detectors and Associated Equipment*, vol. 422, no. 1, pp. 929–932, 1999.

[2] J. Chin, A. Forster, C. Clerici, L. Sung, M. Oudina, and K. Rice, "Temperature and humidity aging of poly(p-phenylene-2,6-benzobisoxazole) fibers: Chemical and physical characterization," *Polymer Degradation and Stability*, vol. 92, no. 7, pp. 1234–1246, 2007.

[3] P. Schillebeeckx, B. Becker, Y. Danon, K. Guber, H. Harada, J. Heyse, A. R. Junghans, S. Kopecky, C. Massimi, M. C. Moxon, N. Otuka, I. Sirakov, and K. Volev, "Determination of resonance parameters and their covariances from neutron induced reaction cross section data," *Nuclear Data Sheets*, vol. 113, no. 12, pp. 3054–3100, 2012.

[4] J. M. Carpenter, "Pulsed spallation neutron sources for slow neutron scattering," *Nuclear Instruments and Methods*, vol. 145, no. 1, pp. 91–113, 1977.

[5] J. R. Copley and T. J. Udovic, "Neutron time-of-flight spectroscopy," *Journal of research of the National Institute of Standards and Technology*, vol. 98, no. 1, pp. 71–97, 1993.

[6] G. Song, J. Y. Y. Lin, J. C. Bilheux, Q. Xie, L. J. Santodonato, J. J. Molaison, H. D. Skorpenske, A. M. Dos Santos, C. A. Tulk, K. An, A. D. Stoica, M. M. Kirka, R. R. Dehoff, A. S. Tremsin, J. Bunn, L. M. Sochalski-Kolbus, and H. Z. Bilheux, "Characterization of crystallographic structures using bragg-edge neutron imaging at the spallation neutron source," *Journal of Imaging*, vol. 3, no. 65, 2017.

[7] E. Roessl and R. Proksa, "K-edge imaging in x-ray computed tomography using multi-bin photon counting detectors," *Physics in Medicine & Biology*, vol. 52, no. 15, 2007.

[8] R. F. Barber, E. Y. Sidky, T. G. Schmidt, and X. Pan, "An algorithm for constrained one-step inversion of spectral ct data," *Physics in Medicine & Biology*, vol. 61, no. 10, 2016.

[9] M. Firsching, D. Niederlohner, T. Michel, and G. Anton, "Quantitative material reconstruction in ct with spectroscopic x-ray pixel detectors–a simulation study," in *IEEE Nuclear Science Symposium Conference Record*, 2006, vol. 4, pp. 2257–2259.

[10] T. Balke, A. M. Long, S. C. Vogel, B. Wohlberg, and C. A. Bouman, "Hyperspectral neutron ct with material decomposition," in *IEEE International Conference on Image Processing (ICIP)*, 2021, pp. 3482–3486.

[11] A. S. Losko and S. C. Vogel, "3d isotope density measurements by energy-resolved neutron imaging," *Scientific Reports*, vol. 12, pp. 6648, 2022.

[12] E. Ametova, G. Burca, S. Chilingaryan, G. Fardell, J. S. Jørgensen, E. Papoutsellis, E. Pasca, R. Warr, M. Turner, W. R. B. Lionheart, and P. J. Withers, "Crystalline phase discriminating neutron tomography using advanced reconstruction methods," *Journal of Physics D: Applied Physics*, vol. 54, no. 32, 2021.

[13] V. P. Pauca, J. Piper, and R. J. Plemmons, "Nonnegative matrix factorization for spectral data analysis," *Linear Algebra and its Applications*, vol. 416, no. 1, pp. 29–47, 2006.

[14] X. Wang, A. Sabne, S. Kisner, A. Raghunathan, C. A. Bouman, and S. Midkiff, "High performance model based image reconstruction," *Association for Computing Machinery*, vol. 51, no. 8, 2016.

[15] J. Y. Y. Lin and G. Song, "bem: modeling for neutron bragg-edge imaging," *Journal of Open Source Software*, vol. 3, no. 30, pp. 973, 2018.